# The 2021 Mw6.7 Lake Hovsgol, Mongolia earthquake: Irregular normal faulting with slip partitioning controlled by an adjacent strike-slip fault

Yuqing He[1], Teng Wang[2], and Li Zhao[2]

[1]Peking university
[2]Peking University

November 23, 2022

**Abstract**

We reveal a slip-partitioning rupture on the North Hovsgol Fault during the 2021 Mw6.7 Lake Hovsgol, Mongolia earthquake. Left-lateral motions on the Mondy Fault north of the epicenter likely controlled the observed slip partitioning pattern. The earthquake highlights the non-negligible role of the bounding strike-slip fault in the formation and evolution of oblique rift.

# The 2021 Mw6.7 Lake Hovsgol, Mongolia earthquake: Irregular normal faulting with slip partitioning controlled by an adjacent strike-slip fault

**Yuqing He[1], Teng Wang[1], Li Zhao[1]**

[1]School of Earth and Space Sciences, Peking University, Beijing 100089, China.

Corresponding author: Teng Wang (wang.teng@pku.edu.cn)

## Key points:

- We reveal a slip-partitioning rupture on the North Hovsgol Fault during the 2021 Mw6.7 Lake Hovsgol, Mongolia earthquake.
- Left-lateral motions on the Mondy Fault north of the epicenter likely controlled the observed slip partitioning pattern.
- The earthquake highlights the non-negligible role of the bounding strike-slip fault in the formation and evolution of oblique rift.

## Abstract

In transtensional regions, structures striking obliquely to the extension direction generally exhibit oblique or partitioned slips. However, their on-fault partitioning patterns and controlling factors are less known, hindering our understanding of the evolution of rifting process. Here we study the slip distribution of the 2021 Mw6.7 Lake Hovsgol, Mongolia earthquake occurred in a pull-apart basin using InSAR observations. Our preferred slip model shows a remarkable feature with three zones exhibiting distinct slip directions at different depths. The Coulomb stress change analysis reveals that this pattern is likely controlled by the left-lateral motion on the Mondy Fault to the north, which also inhibits the growth of a boundary fault to the east of the lake, shaping the asymmetric graben structure in this region. Our results imply the important role of major strike-slip faults bounding the pull-apart basin in the formation and evolution of the oblique rift.

## Plain Language Summary

In a tensional regime, accumulated stress is mainly released by normal-faulting events, whereas when the fault is oriented obliquely to the direction of maximum extension, slip partitioning likely occurs. The 2021 Mw6.7 Lake Hovsgol, Mongolia earthquake provides a rare opportunity for studying the fault slip that is oblique to the direction of regional extension. We obtain the coseismic deformation of this event using both ascending and descending InSAR observations. Our result shows that the slips are partitioned on the graben-boundary fault in both strike and dip directions, aided by the stress changes from a nearby major strike-slip fault. The role of the boundary strike-slip fault around the pull-apart basin is significant in the oblique rift regime, as it likely controls the behavior of the graben-boundary fault and affects the evolution of the graben.

## 1 Introduction

Pull-apart basins are topographic depressions due to the presence of extension from two or more (en echelon) strike-slip fault systems and are bounded by diagonal transfer faults on their ends (e.g., Rahe et al., 1998; Alper, 2010; Gürbüz, 2010). In a pull-apart basin, one common structure is a half graben bounded by a master normal fault on one side and a domain of hanging-wall beds dipping toward the master fault on the other side (e.g., Groshong, 1989; Ring, 1992). Accompanied by crustal thinning, a pull-apart basin may evolve into a rift zone (e.g., Mann et al., 1983; Gartman and Hein, 2019). During this process, oblique slips generally occur on the basin side at the ends of the en echelon faults due to the transtensional movement (Rodgers, 1980), which is characterized by an irregular normal-slip fault at the basin margin (e.g., Crowell, 1974; Ring, 1992; Taghipour et al., 2018). Such irregular normal-slip faults play an important role in the formation and evolution of rift zones (e.g., Lavier, 2002).

The Baikal Rift Zone (BRZ; e.g., Seminsky, 2009) is a SW-NE-oriented active rift in the Mongol-Siberian mountainous area (Figure 1). Previous studies proposed that the BRZ and its associated shear zone are related to both local sinistral shear and, on a larger scale, the far-field India-Eurasia collision in the Eocene time (e.g., Tapponnier and Molnar, 1977, 1979; Hutchinson et al., 1992; Mats, 1993). In southwestern BRZ, the en echelon left-stepping, left-lateral strike-slip faults, including the Bolnay Fault (BF) in the south and the Mondy Fault (MF) in the north (Figure 1), foster a pull-apart tensional environment in northwestern Mongolia. Earthquakes with normal and strike-slip mechanisms prevailed in this region (Klyuchevskii and Dem'yanovich, 2004; Figure 1a). The Hovsgol basin in southwestern BRZ is oriented approximately perpendicular to the Tunga depression and the South Baikal basin (Krivonogov and Safonova, 2016). Formed in the Pliocene, it is a typical half graben bounded by the Hovsgol Fault system near the termination of the Mondy Fault (e.g., Zolotarev et al., 1982; Zorin et al., 1989; Orkhonselenge et al., 2013). Although historical earthquakes showed mixed mechanisms with a significant amount of rift-related normal slip surrounding Lake Hovsgol (Golenetsky and Misharina, 1978; Demberel and Klyuchevskii, 2017; Figure 1a), events with near-field observations are rare, hindering our understanding of the strain release mechanism in the transtensional regime and its implication to the evolution of half-graben structure.

On 11 January 2021, an Mw6.7 earthquake shocked the Lake Hovsgol basin, which is the largest event that has been instrumentally recorded in this region. Aftershocks within two months after the mainshock distributed trending NW on the west bank of the lake (Figure 1a). Four months later, an Mw5.6 earthquake occurred nearby with a similar focal mechanism but at a greater depth (see Table S1 in the Supporting Information). Focal mechanisms from the USGS, gCMT, and GFZ showed normal faulting with a significant strike-slip component (Table S1). The predominant double-couple component (~97% from USGS) suggests that this event was likely to rupture on a single fault plane. Field survey indicated that projections of the east-dipping nodal planes from different sources correlate well with the mapped old scarp of the Hovsgol Fault, yet with no observable coseismic surface rupture on lake banks (Battogtokh et al., 2021). Results from joint inversions using single-track InSAR and teleseismic data (Liu, G. et al., 2021; Liu, X. et al., 2021) showed that the rupture fault was located between the West Range and the Doloon Uul Peninsula, oblique to the direction of maximum extension (Figure 1b). For such a configuration, fault slip partitioning likely occurs (Philippon et al., 2015).

Slip partitioning in oblique rifting has been studied based on the inversions of seismic data (e.g., Fanavoll and Lippard, 1994), field-based observations (e.g., Rao et al., 2017), and stress analog modeling (e.g., Brune, 2014). However, the relation between the fault slip distribution and regional stress regime is less investigated. The 2021 Mw6.7 Lake Hovsgol event provides a chance to probe the detailed slip distribution of an earthquake occurring near the termination of a major strike-slip fault that promotes the development of a pull-apart basin. So far, the available slip distribution models for the 2021 Mw6.7 event suffer from significant uncertainties due to the single geometry constraint of InSAR (e.g., Liu, G. et al., 2021; Liu, X. et al., 2021), preventing a deep discussion about its slip-partitioning pattern and the mechanism behind.

In this study, we use InSAR observations from both descending and ascending geometries to obtain the fault geometry and slip distribution of the 2021 Mw6.7 Lake Hovsgol earthquake. Our model shows that strike and normal slips occurred at distinct asperities on a fault plane dipping ~53° to the northeast. By applying a simple Coulomb stress analysis based on the elastic dislocation model, we find that the slip partitioning is likely controlled by motions on the left-lateral strike-slip Mondy Fault ~50 km north of the epicenter. The resulting stress change from the Mondy Fault also inhibits the formation of a west-dipping boundary fault east of Lake Hovsgol, sculpting the half-graben structure. Our results reveal the important role of transform strike-slip faults in controlling the seismicity and tectonic evolution of a pull-apart basin, shedding new lights on the understanding of oblique slip partitioning in transtensional regimes.

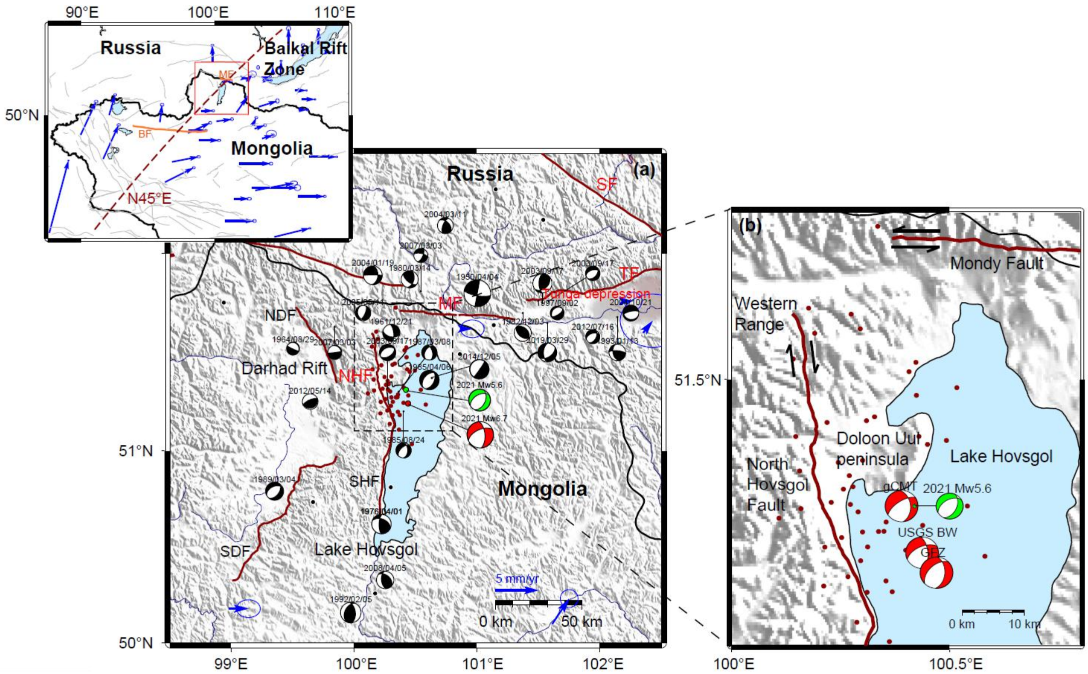


**Figure 1.** Tectonic settings and historical earthquakes around the southwestern Baikal Rift Zone (BRZ). In the top-left plot, the red box shows the study area, while blue arrows depict the GPS horizontal velocities with 95% confidence ellipses from Calais et al. (2003). Gray lines represent the active faults from Styron and Pagani (2020), whereas orange lines highlight the Mondy Fault (MF) and Bolnay Fault (BF). (a) Map of the study area. The red and green beachballs display USGS focal mechanisms of the 2021 Mw6.7 Lake Hovsgol and 2021 Mw5.6 earthquakes, respectively. Black beachballs indicate historical seismicities from previous studies (Khilko et al., 1985; Delouis et al., 2002; Melnikova et al., 2013; Dobrynina et al., 2018). Dark red dots show aftershock locations from USGS within two months after the Mw6.7 earthquake. Dark red lines depict active faults in the southwestern BRZ. The main active faults in this region include the North Hovsgol Fault (NHF), South Hovsgol Fault (SHF), North Darhad Fault (NDF); South Darhad Fault (SDF); Tunga Fault (TF), and Sayan Fault (SF). (b) Enlarged view of the dashed black box in (a) showing the northern Lake Hovsgol with focal mechanisms of the Mw6.7 event from different sources.

## 2 Coseismic deformation mapping

Three interferograms from the descending Sentinel-1 and ascending ALOS-2 satellites covering the earthquake area are obtained to derive the surface deformation field of the 2021 Mw6.7 event (Figure 2; Table S2). These interferograms consistently suggest a complex rupture rather than a simple normal-faulting event.

The descending Sentinel-1 interferogram captures the complete deformation field. A striking feature is that the dense fringes distributed northwest of Lake Hovsgol are separated by the North Hovsgol Fault (NHF). Particularly, east of the NHF, two distinct centers indicate that the whole area moved away from the satellite along the

LOS direction with the maximum deformation reaching ~0.3 m. South of these dense fringes, a slight slant-range shortening is distributed on both banks of Lake Hovsgol.

Two tracks of ascending ALOS-2 interferograms show the deformation field from the other geometry. The two deformation centers east of the NHF clearly indicate that this area also moved away from the ascending LOS direction, suggesting a subsidence. However, west of the NHF, a LOS lengthening can be identified, showing a different pattern from the descending interferogram. In addition, the east bank of Lake Hovsgol slightly moved away from the satellite, again in contrast to the descending observation, indicating that the deformation in these areas is dominated by horizontal movements.

Compared with previous studies (Liu, G. et al., 2021; Liu, X. et al., 2021), the combination of ascending and descending measurements allows us to derive the coseismic deformation in both vertical and east-west directions (Figures 2d&2e; Table S3). The decomposition indicates that the dense fringes east of the NHF are a combination of subsidence (~0.4 m) and eastward movement (~0.15 m), while on its west side, westward deformation (~0.16 m) dominates without an obvious vertical motion, reflecting the tensional feature of this event superimposed with local slips across the NHF.

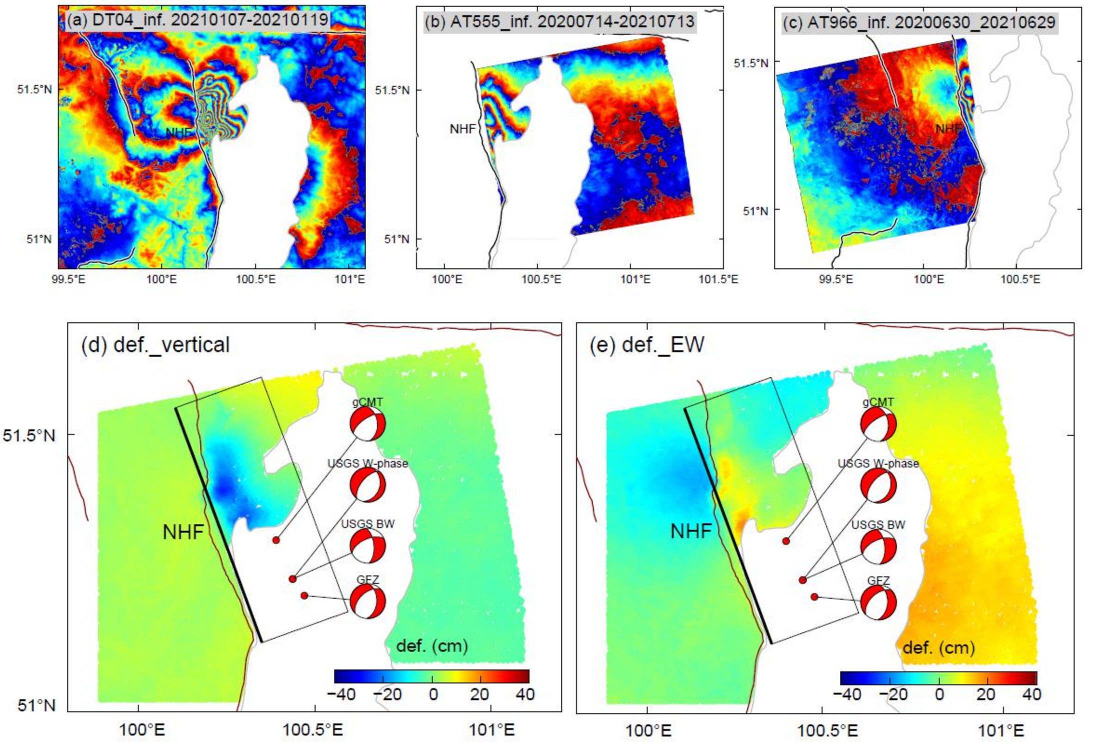


**Figure 2.** Surface deformation associated with the 2021 Mw6.7 Lake Hovsgol earthquake obtained from Sentinel-1 and ALOS-2 SAR satellites. The water body has been masked out manually. (a-c) Interferograms from descending Sentinel-1 (DT04) and ascending ALOS-2 (AT555 and AT966) tracks, respectively. (d-e) Vertical and east-west horizontal displacements computed using the observations in (a-c). The reddish color indicates the uplift/eastward movement, while bluish is the subsidence/westward movement. The black rectangle represents the surficial projection of our fault model. The beachballs display focal mechanisms of the Mw6.7 event from different institutions as indicated.

# 3 Fault geometry and slip-distribution model

The ascending and descending deformations are downsampled using the quadtree decomposition algorithm (Jonsson et al., 2002). Based on the aftershock distribution, geological information and InSAR deformation field, we conclude that the most likely rupture fault of this event is the NW-SE trending NHF. With a fixed fault location, we search for the model parameters using the Geodetic Bayesian Inversion Software (Bagnardi and Hooper, 2018). The best-fitting fault plane follows the shallow NHF dipping ~53° to the northeast. The uniform slip model favors normal slip with a significant right-lateral strike-slip component (see Table S4 for detailed inversion results).

To obtain the coseismic slip distribution, we extend the fault plane to 50 km × 30 km in strike and dip directions, respectively, and discretize it into patches with a size of 2 km × 2 km. We invert for the slip distribution using the steepest descent method (Wang et al., 2009). Figure 3 shows the resulting slip distribution on our optimal fault plane and data fitness. The model fits the main features of the displacement field quite well (Figures 3e-m), with a correlation coefficient of ~97%. The dimensionless misfits for ascending and descending deformation fields are 1.2 and 0.8, respectively. Considering a shear modulus of 30 GPa, the individual seismic moments attributed to the dip-slip and strike-slip components are $1.18\times10^{19}$ N·m (corresponding to Mw6.68) and $5.76\times10^{18}$ N·m (corresponding to Mw6.47), respectively, which means that the accumulated transtensional stress is released at different crustal depths as dip and strike slips with a ratio of 2 between them. The estimated total seismic moment is $1.316\times10^{19}$ N·m, corresponding to Mw6.71, which agrees with the previous solutions (Table S1).

Overall, our slip model shows that the slip is partitioned into three areas at different depths on the fault plane with different mechanisms (Figures 3a-d). Specifically, purely right-lateral slips are apparent at a shallow depth of 0-5 km bracketed by two oblique-slip patches below 5 km with a slip amount of ~1.5 m. The slips terminate at the two ends of the mapped NHF. Though complicated, the focal mechanism estimated from our slip distribution agrees with those from other institutions (beachballs in Figure 3a), supporting the observed slip-partitioning pattern.

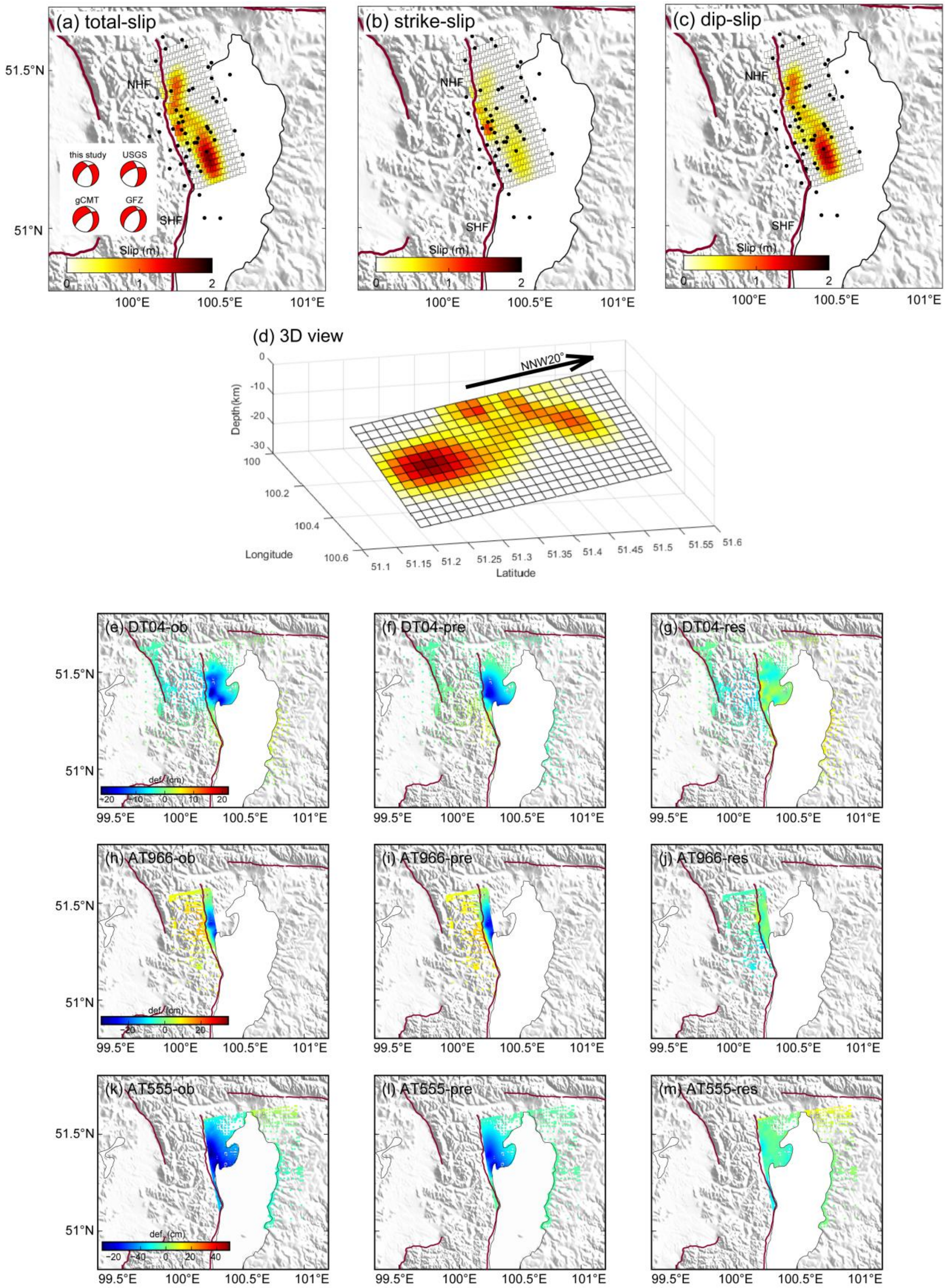


**Figure 3.** Fault slip distribution and data fitness of the preferred fault model. (a-c) Total, strike and dip slips of the optimal fault model, respectively. The black dots represent aftershocks within 2 months after the mainshock. The beachballs in (a) display focal mechanisms of the Mw6.7 event from this study, USGS, Global CMT, and GFZ. (d) The 3-D

view of the fault slip distribution. (e-m) Observed, predicted, and residual maps based on our preferred model with track numbers indicated on the top.

# 4 Stress change analysis

To investigate the role of the nearby Mondy Fault (MF) in affecting the observed slip-partitioning pattern on the NHF, we conduct a simple dislocation modeling in an elastic half space (Okada, 1985; 1992) with constraints from field observations and historical earthquakes. We assume a left-lateral slip of 1 m occurring on the EW-trending Mondy Fault from the surface down to 30-km depth in accordance with the slip during the 1950 Mw6.9 Mondy event based on the empirical relation between slip and magnitude (Wells and Coppersmith, 1994) as well as the GPS velocity at the Mondy station (Calais et al., 2003). By doing so, we have in fact assumed that the slip pattern of the 1950 earthquake represents the long-term motion of the Mondy Fault. Then, we calculate the Coulomb, shear and normal stress changes on the NHF for dip-slip and strike-slip mechanisms due to slips on the Mondy Fault (Figures 4 & S1).

As expected, when assuming a normal-faulting mechanism on the NHF, the Coulomb stress changes are overall positive (Figure 4a&4d), promoting normal slips as revealed in our slip model. However, assuming a right-lateral mechanism on the NHF, the positive Coulomb stress change only occurs in the middle section of the NHF, remarkably consistent with the distribution of a dextral strike-slip component (Figures 4b&4e). Moreover, negative Coulomb stress changes appear at two ends of the NHF, which may prevent the propagation of the strike slip during the 2021 event. Therefore, the rupture pattern of the 2021 event is likely facilitated or even controlled by the slips on the Mondy Fault. In other words, the NHF has accumulated transtensional strains non-uniformly, with a purely right-lateral shear strain at a shallow depth, which were released simultaneously during the 2021 Mw6.7 earthquake.

We also examine the Coulomb stress changes resulted from the motion of Mondy Fault on a symmetrically oriented, west-dipping normal fault (dark red dash line in Figure 4c) to the east of Lake Hovsgol. It is clear that the stress resulted from the motion on Mondy Fault prevents a normal faulting on the assumed west-dipping fault, and the stress suppression is even stronger at greater depth (Figures 4c&4f). We thus propose that the strike-slip Mondy Fault may inhibit the initiation and growth of a west-dipping normal fault east of Lake Hovsgol, thus shaping the half-graben structure.

Note that due to the inaccessibility of this region, different studies show variant mapped traces of the Mondy Fault (Table S5). We conduct Coulomb stress analysis based on the fault traces from Liu, G. et al. (2021) and GAF-DB (Styron and Pagani, 2020) (Figures S1-S5). It is clear that when utilizing the middle and eastern segments of the former one, the distribution of the stress changes matches best with the slip distribution. Granted, many other factors may lead to the spatially partitioned slip pattern as well, such as frictional behavior (e.g., French and Condit, 2019), fault geometry (e.g., Kobayashi et al., 2018), crustal heterogeneity (e.g., Smith and Mosley, 1993; Ring, 1994), pre-existing asperity (e.g., Petit, 1996), and a deep-seated weak zone striking obliquely to the extension direction (e.g., Corti et al., 2013; Osagiede et al., 2021). Precisely determined fault geometry, slip rates, and paleo-stress analysis are needed to further quantify the transtensional strain for better understanding the fault development and structure evolution in actively transtensional regions. Nevertheless, the remarkable consistency of the Coulomb stress distribution with the coseismic slip pattern is hardly a coincidence and strongly suggests that the Mondy Fault plays an important role in the coseismic slip partitioning on the NHF.

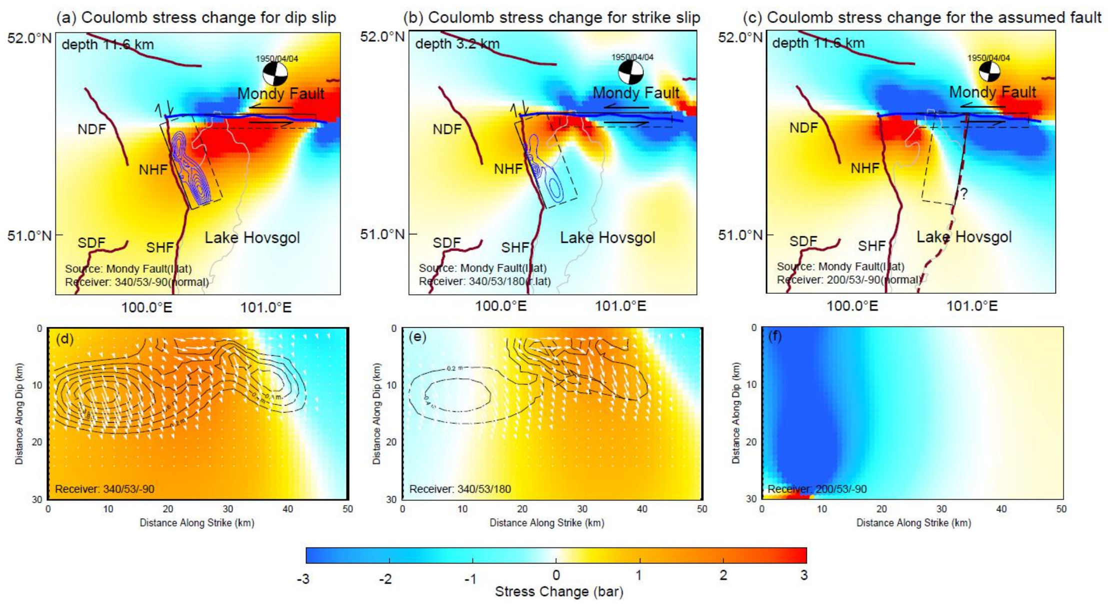


**Figure 4.** Stress change analysis based on a simple dislocation model applied on the Mondy Fault indicated by the blue line (Liu, G. et al., 2021). Warm (cold) color means facilitating (inhibiting) slips on the receiver faults. The beachball displays focal mechanism of the 1950 Mw6.9 Mondy earthquake (Delouis et al., 2002). (a-c) Map views of the consequent Coulomb stress changes for purely dip and strike slips on the NHF, and for normal slip on an assumed west-dipping fault east of Lake Hovsgol, respectively. For (a) and (b), the stress changes are calculated at the depths of 11.6 km and 3.2 km, respectively, where maximum dip and strike slips occur in our slip model. The blue contours show the dip and strike slips, respectively. The depth for (c) is the same as in (a). The dark red dash line represents the trace of the assumed west-dipping normal fault. Black rectangles represent the surface outlines of the source and receiver faults, respectively, with solid lines showing the upper boundaries. (d-f) Coulomb stress changes on the receiver fault planes as (a-c). The black contours show the coseismic dip and strike slips, respectively. The white arrows represent the slip directions of the fault patches depicted in Figure 3.

# 5 Discussion and conclusions

The most prominent feature of the 2021 Mw6.7 Lake Hovsgol earthquake is the three asperities exhibiting distinct slip mechanisms at different depths on a single fault plane. It displays an interesting strain release pattern starting from deep oblique slips in the south, drastically changing to the shallow right-lateral slips in the middle, and ending up in oblique slips at depth again in the north. Our slip model is consistent with the results derived from descending InSAR and teleseismic data (Liu, G. et al., 2021), but reveals more details of the slip-partitioning pattern, particularly in the northern part of the fault, thanks to the additional constraints from ascending InSAR observations.

In transtensional regions, the accumulated strain can be released separately by normal and strike-slip events, such as earthquakes occurred in the Minto Flats Fault Zone in Central Alaska (Tape et al., 2015) and Lake Tahoe in the Sierra Nevada-Great Basin (Schweickert et al., 2004); by an event with a uniformly oblique slip, such as the 2016 Mw5.9 Zaduo (Qinghai, China) earthquake (Jiang et al., 2018); or in the form of simultaneous ruptures of dip-slip and strike-slip motions in a multi-fault system, such as the 2016 Mw7.0 Kumamoto (Japan) earthquake (Toda et al., 2016) and the 2001 Mw7.8 Kokoxili (Qinghai, China) earthquake (King et al., 2005). Note that in the third catalog, the oblique motion is commonly partitioned into slips on two or more faults with different mechanisms (Fitch, 1972), and the slip partitioning is resulted from the elastoplastic upward propagation of an oblique slip at depth (Bowman et al., 2003; King et al., 2005). However, the 2021 Mw6.7 Lake Hovsgol event occurred on a boundary fault of the pull-apart basin with no obvious slip-partitioned surface break (Battogtokh et al., 2021). The co-existence of strike and normal slips on a single fault plane thus exhibits a different slip-partitioning pattern.

Structures striking obliquely to the extension direction generally exhibit oblique slips or partitioned slips to compensate the accumulated stress (e.g., Withjack and Jamison, 1986; Tron and Brun, 1991; Philippon et al., 2015). It is widely accepted that complex tectonic backgrounds and inhomogeneous stress fields in source regions lead to oblique slips during earthquakes on graben-boundary faults, which has been observed in active oblique rift systems (e.g., Strecker et al., 1990; Ring, 1994; Bonini et al., 1997; Titus et al., 2002; Rao et al., 2017; Liu, G. et al., 2021). Liu, G. et al. (2021) suggested that the reduced NS convergence across the Hovsgol basin may be attributed to the normal faulting with a dextral strike-slip component in this region, consistent with the right-lateral strike slip seen on the ruptured fault. However, the controlling factors to the specific slip pattern on the fault plane are still unknown.

To reveal the mechanism of dip and strike slips partitioning on a bending fault for the 2014 Northern Nagano (Japan) earthquake, Kobayashi et al. (2018) proposed that the shallow slip partitioning may be accounted for by the shear stress resulted from an oblique fault at depth. However, we do not have sufficient evidence for an oblique fault or detachment plane under the seismogenic fault in the Hovsgol basin. We have instead investigated the stress distribution on the graben-boundary fault resulted from the major strike-slip fault. Our results reveal that shallow stress changes from the Mondy Fault contribute to the inhomogeneous shear and normal stress accumulations on the ruptured fault plane, fostering a slip partitioning. On the east coast of the lake, the stress resulted from the Mondy Fault inhibits the development of a west-dipping normal fault, consistent with the asymmetric graben structure of Lake Hovsgol. Our stress analysis suggests that spatially partitioned slips on the graben-boundary fault can result from not only the regional extension but also the local stress change from the adjacent, major strike-slip fault. Similar strain release mode may occur in other transtensional regions with shallow strike slips causing unexpected damages in pull-apart basins, which requires more attention in seismic hazard assessments.

To conclude, coseismic slip partitioning of right-lateral strike-slip and normal faulting is observed on an east-dipping graben-boundary fault during the 2021 Mw6.7 Lake Hovsgol earthquake. Based on a stress analysis, we infer that left-lateral strike slips on the Mondy Fault to the north likely controlled the slip distribution of this event. Motions on the Mondy Fault also pose a restraining stress on the east boundary of Lake Hovsgol, facilitating the formation of the half-graben structure. The 2021 Mw6.7 Lake Hovsgol event thus represents an interesting case of slip partitioning on a single fault associated with an oblique pull-apart basin, and highlights the non-negligible role of the shallow stress resulted from the boundary strike-slip fault. Our result has important implications for understanding the strain release mechanism in oblique extensional tectonic settings and improving the assessment of geohazards.

# Acknowledgments

The authors are grateful for insightful discussions with Heng Luo and Zhen Li from Peking University, China, and Taewook Kim from Kangwon National University, Korea. This work has been supported by the National Natural Science Foundation of China (Grants U1939202 and 41974017).

# Data Availability Statement

All data used in this study are open access. Sentinel-1 SAR images were copyrighted by the European Space Agency (ESA; https://scihub.copernicus.eu/dhus/), and processed by the Sentinel-1 Interferometry Processor software (available at http://sarimggeodesy.github.io/software). The SAR images from ALOS-2 were downloaded from Japan Aerospace Exploration Agency (JAXA; https://gportal.jaxa.jp/gpr/). Focal mechanism solutions come from the U.S. Geological Survey (USGS; https://earthquake.usgs.gov/earthquakes/map/), the Global Centroid Moment Tensor (Global CMT; https://www.globalcmt.org/CMTsearch.html), and the German Research Centre for Geosciences (GFZ; https://www.gfz-potsdam.de/en/). Figures were generated by the Generic Mapping Tools 5.4.3 (http://www.soest.hawaii.edu/gmt/; Wessel et al., 2013). The down-sampled InSAR observations and detailed fault slips are available at https://doi.org/10.5281/zenodo.6551945. All websites were last accessed in May 16, 2022.

# References

Alper, G. Geometric characteristics of pull-apart basins. (2010). *Lithosphere*, 2(3): 199-206.

Bagnardi, M., & Hooper, A. (2018). Inversion of Surface Deformation Data for Rapid Estimates of Source Parameters and Uncertainties: A Bayesian Approach. *Geochem. Geophy. Geosy.* 19(7), 2194-2211.

Battogtokh, D., Bayasgalan, A., Wang, K., Ganzorig, D., Bayaraa, J. (2021). The 2021 Mw 6.7 Khankh earthquake in the Khuvsgul rift, Mongolia. *Mongolian*

*Geoscient.*, 26 (52), 46-61.

Bonini, M., Souriot, T., Boccaletti, M., Brun, J.P. (1997). Successive orthogonal and oblique extension episodes in a rift zone: laboratory experiments with application to the Ethiopian Rift. *Tectonics*, 16, 347-362.

Bowman, D., King, G. and Tapponnier, P. (2003). Slip partinioning by elastoplastic propagation of oblique slip at depth. *Science*, 300, 1121-1123.

Brune, S. (2014). Evolution of stress and fault patterns in oblique rift systems: 3-D numerical lithosphericscale experiments from rift to breakup. *Geochem. Geophys. Geosyst.*, 15, 3392-3415.

Calais, É., Vergnolle, M., San'kov, V., Lukhnev, A.V., Miroshnitchenko, A., Amarjargal, S., & Déverchère, J. (2003). GPS measurements of crustal deformation in the Baikal‐Mongolia area (1994-2002): Implications for current kinematics of Asia. *Journal of Geophysical Research*, 108, 2501. doi: 10.1029/2002JB002373.

Célérier, B. (2008). Seeking Anderson's faulting in seismicity: A centennial celebration. *Reviews of Geophysics*, 46. doi:10.1029/2007rg000240.

Chousianitis, K., Ganas, A., & Evangelidis, C.P. (2015). Strain and rotation rate patterns of mainland Greece from continuous GPS data and comparison between seismic and geodetic moment release. *Journal of Geophysical Research: Solid Earth*, 120, 3909-3931.

Cooke, M.L., Toeneboehn, K., & Hatch, J.L. (2019). Onset of slip partitioning under oblique convergence within scaled physical experiments. *Geosphere*, 16, 875-889.

Corti, G., M. Philippon, F. Sani, D. Keir, and T. Kidane. (2013). Re-orientation of the extension direction and pure extensional faulting at oblique rift margins: Comparison between the Main Ethiopian Rift and laboratory experiments, *Terra Nova*, 25, 396-404.

Crowell, J. C. (1974). Origin of late cenozoic basins in southern california. *Modern & Ancient Geosynclinal Sedimentation*, 57, 190-204.

Delouis, B., J. Deverchere, V. Melnikova, N. Radziminovitch, L. Loncke, C. Larroque,

J. F. Ritz, and V. San`kov. (2002). A reappraisal of the 1950 (Mw 6.9) Mondy earthquake, Siberia, and its relationship to the strain pattern at the south-western end of the Baikal rift zone. *Terra Nova*, 14, 491-500.

Demberel, S., Klyuchevskii, A. (2017). Lithospheric stress in Mongolia, from earthquake source data. *Geosci. Front.*, 8, 1323-1337.

Dem'yanovich, V.M., Klyuchevskii, A.V., & Chernykh, E.N. (2008). Lithospheric stress and strain and the seismicity in the Belin-Busiingol fault zone, southern Baikal region. *Journal of Volcanology and Seismology*, 2, 40-54.

Dobrynina, A.A., Sankov, V.A., Tcydypova, L.R., German, V.I., Chechelnitsky, V.V., & Ulzibat, M. (2017). Hovsgol earthquake 5 December 2014, MW = 4.9: seismic and acoustic effects. *Journal of Seismology*, 22, 377-389.

Dubey, A.K. (2014). Strike-Slip Fault. In: Understanding an Orogenic Belt. *Springer Geology*. Springer, Cham. https://doi.org/10.1007/978-3-319-05588-6_6.

Fanavoll, S., & Lippard, S.J. (1994). Possible oblique-slip faulting in the Skagerrak Graben, as interpreted from high resolution seismic data. *Norsk Geologisk Tidsskrift*, 74, 146-151.

Fitch, T. (1972). Plate convergence, transcurrent faults, and internal deformation adjacent to southeast Asia and the western Pacific, *J. Geophys. Res.*, 77, 4432-4462.

French, M.E., & Condit, C.B. (2019). Slip partitioning along an idealized subduction plate boundary at deep slow slip conditions. *Earth and Planetary Science Letters*, 528, 115828.

Gartman, A., & Hein, J.R. (2019). Mineralization at Oceanic Transform Faults and Fracture Zones. *Transform Plate Boundaries and Fracture Zones*.

Golenetsky, S.I. & Misharina, L.A. (1978). Seismicity and earthquake focal mechanisms in the Baikal rift zone. *Tectonophysics*, 45, 71-85.

Groshong, R. H. (1989). Half-Graben Structures-Balanced Models of Extensional Fault-Bend Folds. *Geological Society of America Bulletin*, 101(1), 96-105.

Gürbüz, A. (2010). Geometric characteristics of pull-apart basins. *Lithosphere*, 2, 199-206.

Hutchinson, D.R., Golmshtok, A.J., Zonenshain, L.P., Moore, T.C., Scholz, C.A., & Klitgord, K.D. (1992). Depositional and tectonic framework of the rift basins of Lake Baikal from multichannel seismic data. *Geology*, 20, 589-592.

Jiang, G., Wen, Y., Li, K., Fang, L., Xu, C., Zhang, Y., & Xu, X. (2018). A NE-Trending Oblique-Slip Fault Responsible for the 2016 Zaduo Earthquake (Qinghai, China) Revealed by InSAR Data. *Pure and Applied Geophysics*, 175, 4275-4288.

Jonsson, S., Zebker, H., Segall, P., & Amelung, F. (2002). Fault slip distribution of the 1999 M-w 7.1 Hector Mine, California, earthquake, estimated from satellite radar and GPS measurements. *Bull. Seismol. Soc. Am*. 92(4), 1377-1389.

Khilko, S. D., R. A. Kurushin, V. M. Kochetkov, L. A. Misharina, V. I. Melnikova, N. A. Gileva, S. V. Lastochkin, I. Baljinnyam, and D. Monkhoo. (1985). Earthquakes and Principles of Seismic Zoning of Mongolia. Nauka, Moscow, 224. (in Russian).

King, G., Klinger, Y., Bowman, D., & Tapponnier, P. (2005). Slip-partitioned surface breaks for the mw 7.8 2001 kokoxili earthquake, china. *Bulletin of the Seismological Society of America*, 95(2), 731-738.

Klyuchevskii, A. V., & Dem'yanovich, V. M. (2006). Stress-strain state of the lithosphere in the southern Baikal region and northern Mongolia from data on seismic moments of earthquakes. *Izvestiya-Physics of the Solid Earth*, 42(5), 416-428.

Kobayashi, T., Morishita, Y., & Yarai, H. (2018). SAR-revealed slip partitioning on a bending fault plane for the 2014 Northern Nagano earthquake at the northern Itoigawa-Shizuoka tectonic line. *Tectonophysics*, 733, 85-99.

Krivonogov, S. K., & Safonova, I. Y. (2017). Basin structures and sediment accumulation in the Baikal Rift Zone: Implications for Cenozoic intracontinental processes in the Central Asian Orogenic Belt. *Gondwana Research*, 47, 267-290.

Lavier, L.L., & Buck, W.R. (2002). Half graben versus large‐offset low‐angle normal fault: Importance of keeping cool during normal faulting. *Journal of Geophysical Research*, 107(B6), 2122. DOI:10.1029/2001JB000513.

Liu, G., Qiao, X., Yu, P., Zhou, Y., Zhao, B., and Xiong, W. (2021). Rupture Kinematics of the 11 January 2021 Mw 6.7 Hovsgol, Mongolia, Earthquake and Implications in the Western Baikal Rift Zone, *Seismol. Res. Lett.* 92 (6): 3318-3326.

Liu, X., Xu, W., Radziminovich, N.A., Fang, N., & Xie, L. (2021). Coseismic Fault Slip and Transtensional Stress Field in the Hovsgol Basin Revealed by the 2021 Mw 6.7 Turt, Mongolia Earthquake. doi: 10.1002/essoar.10507741.1.

Mann, P.J., Hempton, M.R., Bradley, D.C., & Burke, K.C. (1983). Development of Pull-Apart Basins. *The Journal of Geology*, 91, 529-554.

Mats, V.D. (1993). The structure and development of the Baikal rift depression. *Earth-Science Reviews*, 34, 81-118.

Melnikova, V., Gileva, N.A., Arefyev, S.S., Bykova, V., & Seredkina, A.I. (2013). The August 27, 2008, Mw = 6.3 Kultuk earthquake (South Baikal): The stress-strain state of the source area from the aftershock data. *Izvestiya, Physics of the Solid Earth*, 49, 563-576. (in Russian).

Okada, Y. (1985). Surface deformation due to shear and tensile faults in a half-space. *Bulletin of the Seismological Society of America*, 75, 1135-1154.

Okada, Y. (1992). Internal deformation due to shear and tensile faults in a half-space. *Bulletin of the seismological society of America*, 82, 1018-1040.

Orkhonselenge, A., Krivonogov, S.K., Mino, K., Kashiwaya, K., Safonova, I., Yamamoto, M., Kashima, K., Nakamura, T., & Kim, J. (2013). Holocene sedimentary records from Lake Borsog, eastern shore of Lake Khuvsgul, Mongolia, and their paleoenvironmental implications. *Quaternary International*, 290, 95-109.

Osagiede, E. E., Rosenau, M., Rotevatn, A., Gawthorpe, R., Jackson, C. A-L., & Rudolf, M. (2021). Influence of zones of pre-existing crustal weakness on strain localization and partitioning during rifting: Insights from analog modeling using high-resolution 3D digital image correlation. *Tectonics*, 40, e2021TC006970. https://doi.org/10.1029/2021TC006970

Petit, C., J Déverchère, Houdry, F., Sankov, V. A., Melnikova, V. I., & Delvaux, D.

(1996). Present-day stress field changes along the baikal rift and tectonic implications. *Tectonics*, 15(6), 1171-1191.

Philippon, M., Willingshofer, E., Sokoutis, D., Corti, G., Sani, F., Bonini, M., Cloetingh, S. (2015). Slip re-orientation in oblique rifts. *Geology*, 42, 147-150.

Rahe, B., Ferrill, D.A., and Morris, A.P., (1998). Physical analog modeling of pull-apart basin evolution. *Tectonophysics*, 285, 21-40.

Rao, G., He, C., Cheng, Y., Yu, Y., Hu, J., Chen, P., & Yao, Q. (2018). Active Normal Faulting along the Langshan Piedmont Fault, North China: Implications for Slip Partitioning in the Western Hetao Graben. *The Journal of Geology*, 126, 99-118.

Ring, U. (1994). The influence of preexisting structure on the evolution of the Cenozoic Malawi rift (East African rift system). *Tectonics*, 13, 313-326.

Rodgers, D. A. (1980). Analysis of pull-apart basin development produced by en echelon strike-slip faults. *Spec.publ.int.ass.sediment*, 4.

Schweickert, R.A., Lahren, M.M., Smith, K.D., Howle, J.F., & Ichinose, G.A. (2004). Transtensional deformation in the Lake Tahoe region, California and Nevada, USA. *Tectonophysics*, 392, 303-323.

Seminsky, K.Z. (2009). Major factors of the evolution of basins and faults in the Baikal Rift Zone: Tectonophysical analysis. *Geotecton*., 43, 486. https://doi.org/10.1134/S001685210906003X.

Smith, M., & Mosley, P. (1993). Crustal heterogeneity and basement influence on the development of the Kenya Rift, East Africa. *Tectonics*, 12, 591-606.

Stich, D., Martín, R., Morales, J., JN López-Comino, & Mancilla, F. (2020). Slip partitioning in the 2016 alboran sea earthquake sequence (western mediterranean). *Frontiers in Earth Science*, 8, 587356. https://doi.org/10.3389/feart.2020.587356

Strecker, M.R., Blisniuk, P.M., Eisbacher, G.H. (1990). Rotation of extension direction in the central Kenya rift. *Geology*, 18, 299-302.

Styron, R., Pagani, M. (2020). The GEM Global Active Faults Database. *Earthquake Spectra*, 36(1_suppl):160-180.

Taghipour, K., Khatib, M.M., Heyhat, M., Shabanian, E., & Vaezihir, A. (2018).

Evidence for distributed active strike-slip faulting in NW Iran: The Maragheh and Salmas fault zones. *Tectonophysics*,742, 15-33.

Tape, C., Silwal, V., Ji, C., Keyson, L.H., West, M.E., & Ruppert, N. (2015). Transtensional Tectonics of the Minto Flats Fault Zone and Nenana Basin, Central Alaska. *Bulletin of the Seismological Society of America*, 105, 2081-2100.

Tapponnier, P., & Molnar, P. (1977). Active Faulting and Tectonics in China. *J. Geophys. Res.* 82(20), 2905-2930.

Tapponnier, P., & Molnar, P. (1979). Active faulting and Cenozoic tectonics of the Tien Shan, Mongolia, and Baykal regions, *J. Geophys. Res.* 84, B7, 3425-3459.

Titus, S. & Fossen, Haakon & Pedersen, R. & Tikoff, B. (2002). Pull-apart formation and strike-slip partitioning in an obliquely divergent setting, Leka Ophiolite, Norway. *Tectonophysics.* 354, 101-119.

Toda, S., Stein, R.S., Sevilgen, Volkan, & Lin, Jian, 2011, Coulomb 3.3 Graphic-rich deformation and stress-change software for earthquake, tectonic, and volcano research and teaching—user guide: U.S. Geological Survey Open-File Report 2011–1060, 63 p., available at https://pubs.usgs.gov/of/2011/1060/

Toda, S., Kaneda, H., Okada, S., Ishimura, D., & Mildon, Z. K. (2016). Slip-partitioned surface ruptures for the Mw 7.0 16 April 2016 Kumamoto, Japan, earthquake. *Earth, Planets and Space*, 68(1), 1-11.

Tomokazu, K., Morishita, Y., & Yarai, H. (2017). SAR-revealed slip partitioning on a bending fault plane for the 2014 Northern Nagano earthquake at the northern Itoigawa-Shizuoka tectonic line. *Tectonophysics*. 733, 85-99.

Tron, V., & Brun, J.P. (1991). Experiments on oblique rifting in brittle-ductile systems. *Tectonophysics*, 188, 71-84.

Wang, R., Diao, F., and Hoechner, A. (2013), SDM-A geodetic inversion code incorporating with layered crust structure and curved fault geometry. Paper presented at 2013 *EGU General Assembly Conference*. Vienna, Austria.

Wells, D. L., Coppersmith, K. J. (1994). New empirical relationships among magnitude, rupture length, rupture width, rupture area, and surface displacement.

*Bull. Seismol. Soc. Am.*, 84(4): 974-1002.

Wessel, P., Smith, W.H., Scharroo, R., Luis, J.F., & Wobbe, F. (2013). Generic Mapping Tools: Improved Version Released. *Eos, Transactions American Geophysical Union*, 94, 409-410.

Withjack, M.O., & Jamison, W.R. (1986). Deformation produced by oblique rifting. *Tectonophysics*, 126, 99-124.

Zolotarev, A.G., Kulakov, V.S., Khilko, S.D. (1982). Khubsugul upland. *Geomorphology of Mongolian People Republic. Proceedings of Join Soviet-Mongolian Scientific-Research Geological Expedition*, *Nauka, Moscow*, 28, 109-122. (in Russian).

Zorin Y.A., Tumtanov E.K., Arvisbaatar N. (1989). Structure of Cenozoic basins of the Prekhubsugul region from gravity data. *Geology and Geophysics*, 10, 130-136. (in Russian).

AGU PUBLICATIONS

[Geophysical Research Letters]

Supporting Information for

# The 2021 Mw6.7 Lake Hovsgol, Mongolia earthquake: Irregular normal faulting with slip partitioning controlled by an adjacent strike-slip fault

Yuqing He[1], Teng Wang[1]*, Li Zhao[1]

[1]School of Earth and Space Sciences, Peking University, Beijing 100089, China.

*Correspondence to: Teng Wang (wang.teng@pku.edu.cn)

**This supplementary file includes:**

Text S1. Geometry and trace of the Mondy Fault

Tables S1 to S5

Figures S1 to S5

**Text S1. Geometry and trace of the Mondy Fault**

There are different mapped traces for the Mondy Fault in previous studies. Liu, G. et al. (2021) used the fault trace digitized from Calais et al. (2003); while Liu, X. et al. (2021) used the data from the GEM Global Active Faults Database (GAF-DB; Styron and Pagani, 2020). As for the uncertainties of fault mapped from field observations, we conducted three sets of experiments using different fault locations and geometric parameters (Table S5) to determine the fault location that can best explain the stress effect of a major strike-slip fault on the boundary fault near its termination. Map views and profiles for the stress change on the NHF when utilizing our fault data (i.e. the middle and eastern segments of the MF from Liu, G. et al. (2021)) are displayed in Figure S1. Map views and profiles for the stress change on the NHF are presented in Figures S2 and S3 when utilizing the fault location from Liu, G. et al. (2021) and in Figures S4 and S5 when utilizing the fault location from GAF-DB.

**Table S1**. Source parameters of the 2021 Mw6.7 Hovsgol earthquake and the Mw5.6 aftershock from different sources.

| Study | Epicenter | Auxiliary Plane 1 | Auxiliary Plane 2 | Depth (km) | Mw | Data |
|---|---|---|---|---|---|---|
| | Latitude/Longitude | Strike/Dip/Rake | Strike/Dip/Rake | | | |
| gCMT[a] | 51.32ºN/100.39ºE | 354º/43º/-143º | 236º/66º/-53º | 13.9 | 6.8 | Seismic |
| USGS$_1$[b] | 51.28ºN/100.44ºE | 16º/32º/-110º | 219º/60º/-78º | 11.5 | 6.74 | W-phase |
| USGS$_2$[b] | 51.28ºN/100.44ºE | 245º/58º/-35º | 356º/61º/-143º | 8 | 6.65 | Body wave |
| GFZ[c] | 51.21°N/100.47°E | 226º/51º/-60º | 4º/47º/-121º | 18 | 6.7 | Seismic |
| CENC[d] | 51.28°N/100.5°E | / | / | 10 | 6.8 | Seismic |
| IPGP[e] | 51.24°N/100.44°E | 358º/46º/-139º | 237º/62º/-52º | 13 | 6.84 | Seismic |
| GSRAS[f] | 51.32°N/100.42°E | 228º/46º/0º | 29º/46º/-103º | 20 | Mb 6.5 | Seismic |
| Liu, G. et al., 2021 | / | 353º/51º/-109º | / | 2-15 | 6.75 | Descending InSAR & Seismic (Nonlinear inversion) |
| Liu, G. et al., 2021 | 51.34°N/100.33°E | 345º/42º/- | / | 2-15 | 6.75 | Descending InSAR & Seismic (Grid search) |
| Liu, X. et al., 2021 | 51.34°N/100.33°E | 341º/54º/-146º | / | 8.9 | 6.75 | Descending InSAR & Seismic |
| This study | / | 340º/53º/-116º | / | / | 6.71 | Descending and ascending InSAR |
| USGS (Mw5.6) | 51.31°N/100.42°E | 25º/46º/-116º | 239º/49º/-66º | 18 | 5.6 | W-phase |

| | | | | | | |
|---|---|---|---|---|---|---|
| gCMT (Mw5.6) | 51.31°N/ 100.43°E | 63º/37º/-50º | 197º/63º/-116 | 27.5 | 5.7 | Seismic |

a) http://www.globalcmt.org/cgi-bin/globalcmt-cgi-bin/CMT5/, last accessed January 21, 2022;
b) https://earthquake.usgs.gov/earthquakes/eventpage/usp000juhz#moment-tensor, last accessed January 21, 2022;
c) http://geofon.gfz-potsdam.de/eqinfo/event.php?id=gfz2020bhxs, last accessed January 21, 2022;
d) https://www.cenc.ac.cn/, last accessed January 21, 2022;
e) IPGP, Institute de Physique du Globe de Paris (available at http://www.ipgp.fr/fr, last accessed January 21, 2022);
f) GSRAS, Geophysical Survey of Russian Academy of Sciences (available at http://www.ceme.gsras.ru/new/ssd_news.htm, last accessed January 21, 2022).

**Table S2.** Parameters of SAR images.

| Event | Satellite | Track | Frame | Mode | Timeline (yyyymmdd) |
|---|---|---|---|---|---|
| Mainshock | Sentinel-1B | 04 | 166 | Descending | 20210107<br>20210119 |
| Mainshock | ALOS-2 | 555 | / | Ascending | 20200714<br>20210713 |
| Mainshock | ALOS-2 | 966 | / | Ascending | 20200630<br>20210629 |
| 2021 Mw5.6 earthquake | Sentinel-1B | 55 | 166 | Ascending | 20210429<br>20210511 |
| 2021 Mw5.6 earthquake | Sentinel-1B | 04 | 419 | Descending | 20210425<br>20210507 |

**Table S3.** LOS projection coefficients for the 3-D deformation decomposition.

| | Mean heading angle (°) | Mean incidence angle (°) | North coef. | East coef. | Vertical coef. | Max. LOS displacement (m) | Min. LOS displacement (m) |
|---|---|---|---|---|---|---|---|
| Ascending1 (AT555) | -10.4586 | 36.3027 | -0.1075 | -0.5822 | 0.8059 | 0.18753 | -0.26227 |
| Ascending2 (AT966) | -11.2252 | 31.4267 | -0.1015 | -0.5114 | 0.8533 | 0.14925 | -0.27026 |
| Descending (DT04) | -164.583 | 33.9736 | -0.1486 | 0.5387 | 0.8293 | 0.069325 | -0.21243 |

**Table S4.** The prior, initial value, maximum posteriori probability solutions and confidence intervals for our single fault model.

| Parameter | Lower | Upper | Initial | Optimal | Mean | Median | 2.5% | 97.5% |
|---|---|---|---|---|---|---|---|---|
| Fault length (m) | 29935 | 50000 | 30000 | 33064.3 | 33189.6 | 32720.9 | 30017.4 | 41402.9 |
| Fault width (m) | 5000 | 20000 | 5000 | 5594.64 | 6055.25 | 5664.36 | 5595.08 | 10179.7 |
| Fault depth (m) | 4000 | 10000 | 5000 | 4632.39 | 5145.04 | 4824.68 | 4132.58 | 9279.32 |
| Fault dip (°) | -70 | -45 | -50 | -52.922 | -49.839 | -48.3797 | -62.285 | -45.1317 |
| Fault strike (°) | 150 | 170 | 160 | 160.115 | 161.503 | 160.873 | 160.033 | 160.553 |
| Fault X (m) | 15000.7 | 15000.7 | 15000.7 | 15000.7 | 15000.7 | 15000.7 | 15000.7 | 15000.7 |
| Fault Y (m) | 20000 | 20000 | 20000 | 20000 | 20000 | 20000 | 20000 | 20000 |
| Fault strike slip (m) | 1.5 | 3.5 | 1 | 1.01138 | 1.12829 | 1.03767 | 1.00131 | 2.27079 |
| Fault dip slip (m) | 1.5 | 3.5 | 1 | 1.00591 | 1.05307 | 1.0184 | 1.0006 | 1.41873 |

**Table S5.** Geometrical parameters of the Mondy Fault (MF) from different sources.

| Study | Latitude (° N) | Longitude (° E) | Length (km) | Width (km) | Depth (km) | Dip (°) | Strike (°) | Rake (°) | Slip (m) |
|---|---|---|---|---|---|---|---|---|---|
| Liu, G. et al. (2021) | 51.58 | 100.14 | 60 | 30 | 0 | 75 | 90 | 0 (left-lateral) | 1 |
| GAF-DB | 51.75 | 100.35 | 60 | 30 | 0 | 75 | 90 | 0 (left-lateral) | 1 |
| This study | 51.6 | 100.6 | 60 | 30 | 0 | 75 | 90 | 0 (left-lateral) | 1 |

Note:

1) The latitude and longitude here refer to the position of the top-left corner of the fault plane, while the depth refers to the top of the fault plane;

2) GAF-DB, available at https://github.com/GEMScienceTools/gem-global-active-faults;

3) This study uses the middle and eastern segments of the MF from Liu, G. et al. (2021).

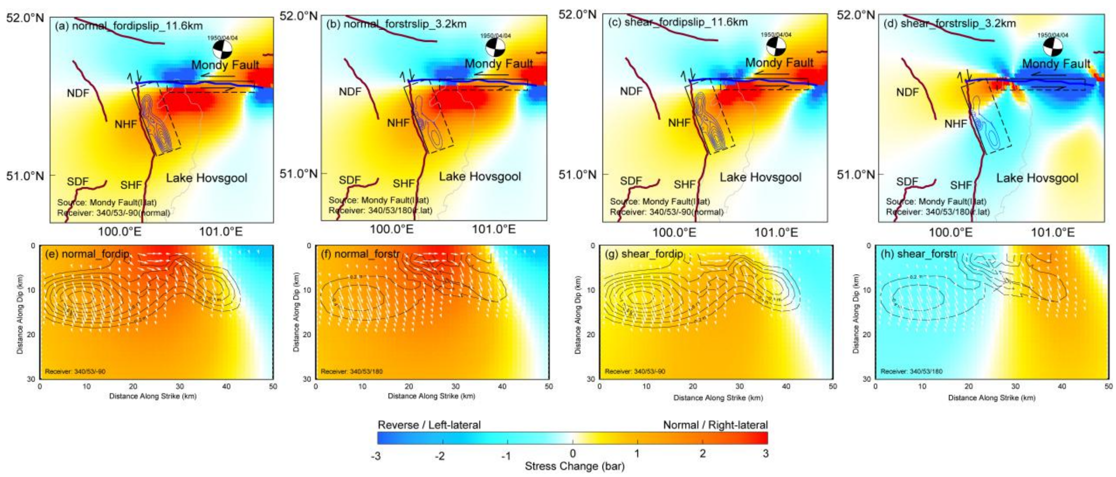


**Figure S1.** The normal and shear stress change analyses for dip and strike slips on the NHF based on the middle and eastern segment of Mondy Fault from Liu, G. et al. (2021). (a-d) Map views of normal and shear stress changes for purely dip and strike slips on the NHF caused by the MF at the depths of 11.6 km and 3.2 km, respectively, where maximum dip and strike slips occur in our slip model. Black rectangles represent the outlines of the NHF and MF, respectively, with solid lines showing the upper boundaries. The blue contours show the dip and strike slips, respectively. (e-h) are related stress change profiles of NHF fault plane based on the (a-d). The black contours show the dip and strike slips, respectively. The white arrows represent the slip directions of the fault patches depicted in Figure 4.

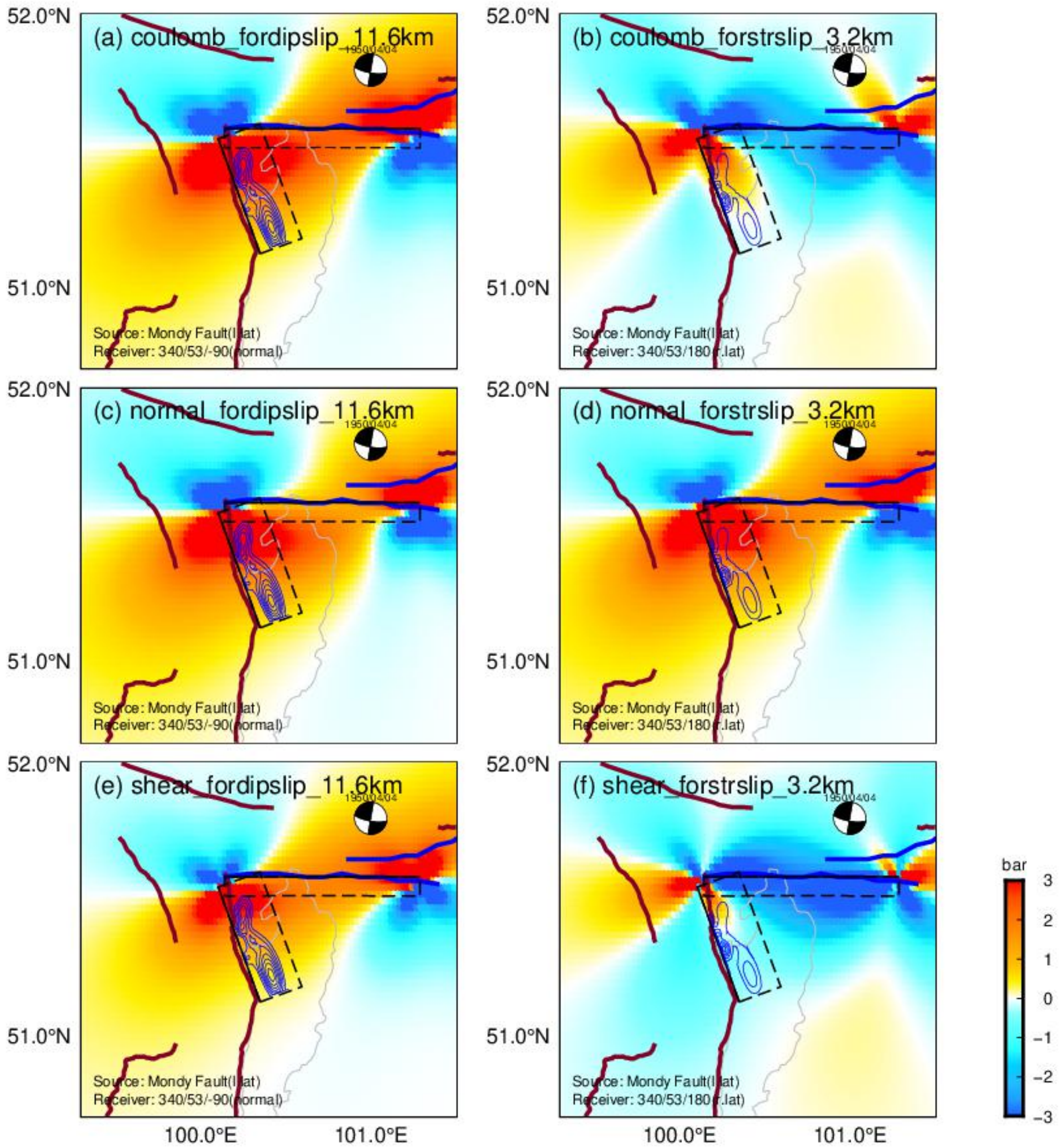


**Figure S2.** The Coulomb (a-b), normal (c-d), and shear (e-f) stress change analyses for dip and strike slips on the NHF based on the Mondy Fault from Liu, G. et al. (2021). The stress changes are calculated at the depths of 11.6 km and 3.2 km, respectively, where the corresponding maximum dip and strike slips occur in our slip model. Blue line represents the fault location of Mondy Fault. Warm (cold) color means facilitating (inhibiting) slips on the receiver faults. Black rectangles show the surface projections of source (MF) and receiver (NHF) fault, respectively, with solid lines showing the upper boundaries.

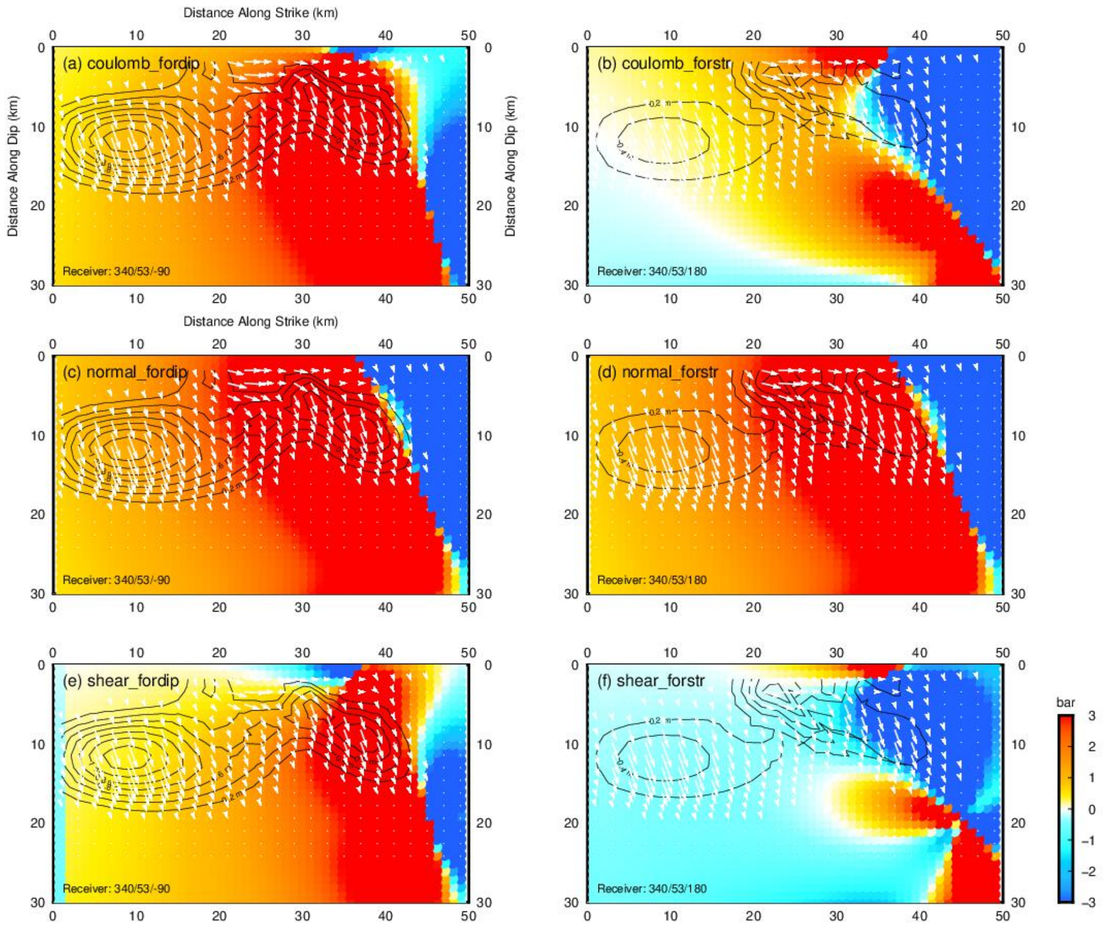


**Figure S3.** The Coulomb (a-b), normal (c-d), and shear (e-f) stress changes on the NHF fault plane according to Figure S2.

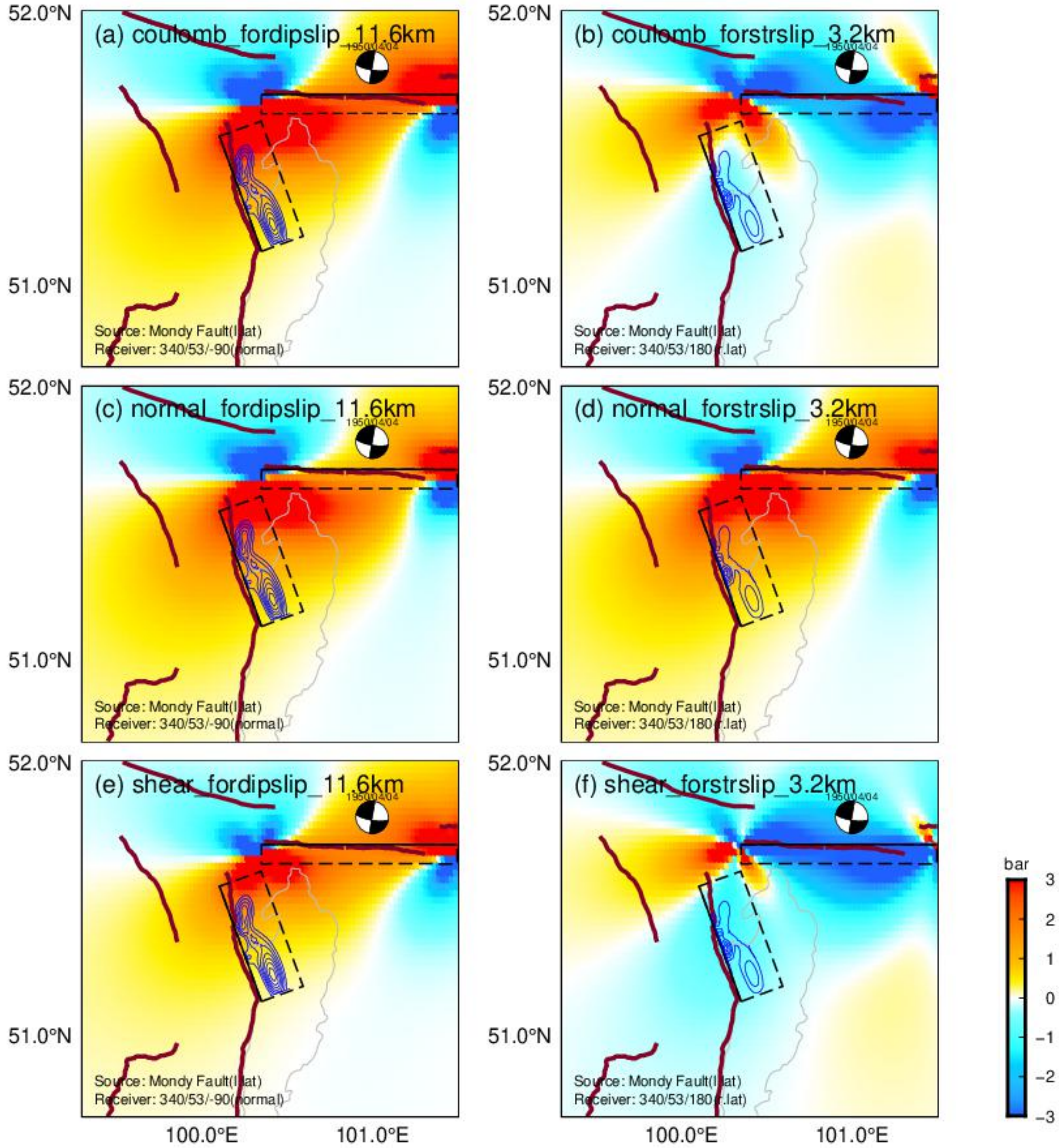


**Figure S4.** The Coulomb (a-b), normal (c-d), and shear (e-f) stress change analyses for dip and strike slips on the NHF based on the Mondy Fault from GAF-DB. The stress changes are calculated at the depths of 11.6 km and 3.2 km, respectively, where the corresponding maximum dip and strike slips occurred in our slip model. The dark-red line represents the fault location of the Mondy Fault. Warm (cold) color means facilitating (inhibiting) slips on the receiver faults. Black rectangles show the surface projections of source (MF) and receiver (NHF) fault, respectively, with solid lines showing the upper boundaries.

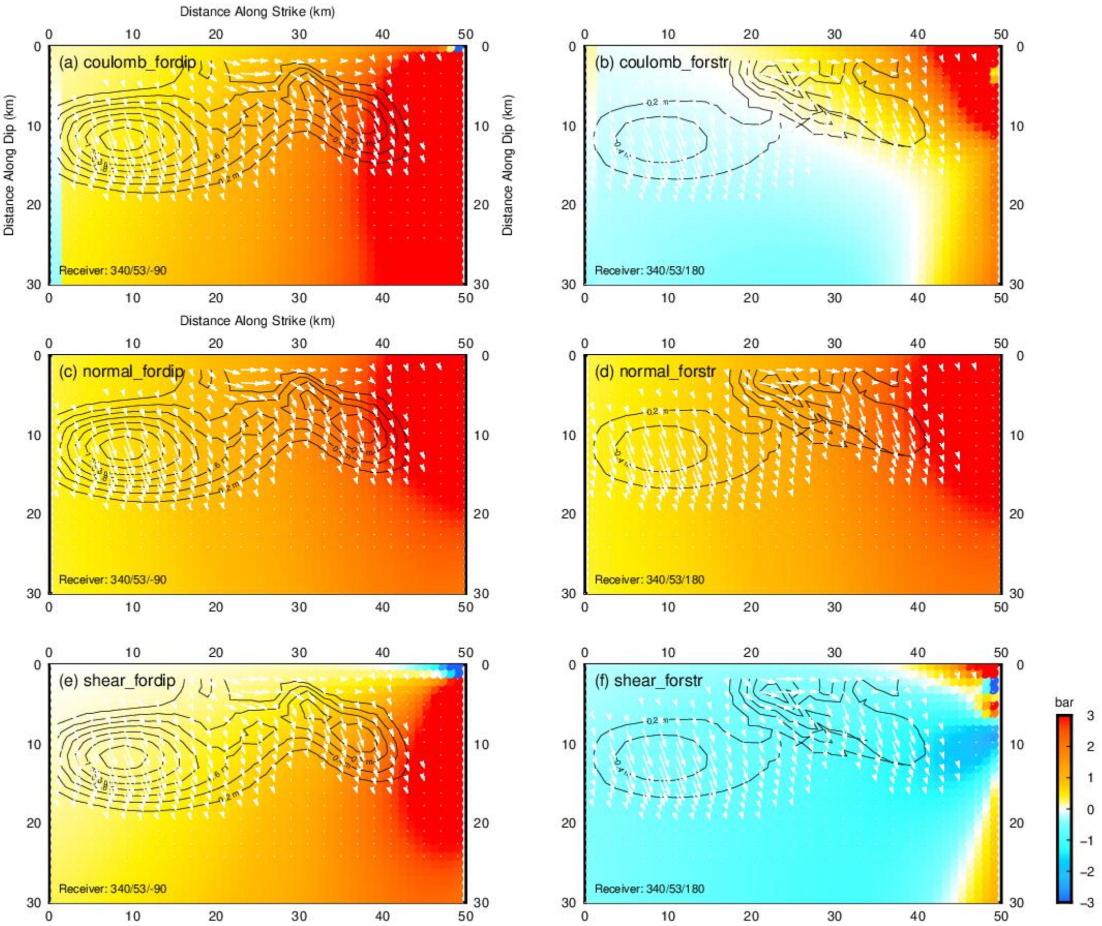


**Figure S5.** The Coulomb (a-b), normal (c-d), and shear (e-f) stress changes on the NHF fault plane according to Figure S4.

## References


Calais, É., Vergnolle, M., San'kov, V., Lukhnev, A.V., Miroshnitchenko, A., Amarjargal, S., & Déverchère, J. (2003). GPS measurements of crustal deformation in the Baikal-Mongolia area (1994-2002): Implications for current kinematics of Asia. *Journal of Geophysical Research*, 108, 2501. doi: 10.1029/2002JB002373.

Liu, G., Qiao, X., Yu, P., Zhou, Y., Zhao, B., & Xiong, W. (2021). Rupture Kinematics of the 11 January 2021 Mw 6.7 Hovsgol, Mongolia, Earthquake and Implications in the Western Baikal Rift Zone. *Seismological Research Letters*, 92 (6): 3318-3326.

Liu, X., Xu, W., Radziminovich, N.A., Fang, N., & Xie, L. (2021). Coseismic Fault Slip and Transtensional Stress Field in the Hovsgol Basin Revealed by the 2021 Mw 6.7 Turt, Mongolia Earthquake. doi: 10.1002/essoar.10507741.1.

Styron, R.H., & Pagani, M. (2020). The GEM Global Active Faults Database. *Earthquake Spectra*, 36, 160-180.